ACS OMEGA

http://pubs.acs.org/journal/acsodf

Article

Crack Evolution and Failure Modes of Shale Containing a Pre-Existing Fissure under Compression

Lin Li, Yuehua Liu, Wei Liu,* Xiong Zhang, Jie Chen, Deyi Jiang, and Jinyang Fan

Cite This: *ACS Omega* 2021, 6, 25461−25475

Read Online

ACCESS | Metrics & More | Article Recommendations

ABSTRACT: To investigate the crack evolution of Longmaxi shales with a single prefabricated fissure, a CCD (charge coupled device) camera and AE (acoustic emission) monitoring equipment were employed. On the basis of real-time CCD photographs and AE events, a real-time crack evolution process in fissured shale specimens under uniaxial compression was investigated. The crack initiation angle and extension angle were calculated, the relationship between the crack initiation stress, strength, and crack angle was compared, and the proportion of tensile and shear cracks at different stages of the whole compression process was briefly analyzed. The results demonstrate that, with the increase in fissure angle (α), the weakening ability of the prefabricated fissure to uniaxial compressive strength and crack initiation stress was reduced. The initial cracks and secondary cracks always appeared at the tip of the pre-existing fissure in the form of tensile cracks for α = 30−90°. The crack initiation angle and expansion angle increased first and then decreased rapidly with α increasing. Furthermore, the ultimate failure modes were mixed tensile and shear failure when α = 0−90°. The crack evolution of the fissured shale was progressive, but the final failure of the fissured specimen occurred rapidly. Furthermore, the appearance of the cracks, stress drops, and AE counts had good consistency in time.

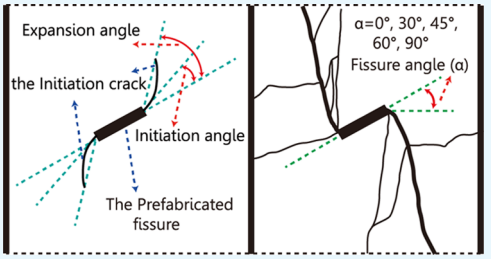

1. INTRODUCTION

Shale gas, as an unconventional oil and gas resource, has abundant reserves and great development potential in China.[1] However, large-scale commercial mining is needed to alleviate China's energy problems.[2] Horizontal well fracturing technology is a common means to form industrial gas reservoirs and improve productivity.[3,4] Perforation orientation is important for the final fracturing effect.[5,6] Shale gas development in China is still in the initial stage from the perspective of development technology and production increase effect.[7] As a typical anisotropic material, shale naturally contains bedding, and a large number of natural joints (fissures) have developed due to various tectonic actions.[8−11] Most studies on the shale reservoir focused on its mechanical properties and mechanism,[12−15] but few focused on the law of fracture initiation and propagation of fractured shale under load (such as fracturing). Generally speaking, the geometry of joints has an important influence on the strength and deformation characteristics of the jointed rock mass.[16−18] The primary joints serve as the reservoir space of shale gas, and the bedding serves as a methane seepage channel. Generally speaking, in the process of shale gas exploitation, the original complex fissure network within a shale matrix under fracturing can promote the fracture degree of the shale reservoir, thus improving the shale gas production efficiency. Therefore, it is of great significance to study the influences of the fissure angle on the cracking behaviors of the shale containing fissures.

Scholars at home and abroad have done a lot of research on the deformation and failure characteristics of the fissured rock mass. Tian and Liu[19] analyzed the relationship between shale deformation and adsorption and elastic properties. Sun and Jin[20] attributed the differences between the observed fracture strength and theoretical cohesive strength of crystals to defects in brittle materials. Hoek and Bieniawski[21] studied the initiation and propagation of a single Griffith fissure under biaxial compression tests. The study of rock failure performance is associated with the study of fracture toughness.[14,22,23] Martin and Chandler[24] thought that the strength of an intact rock consisted of two parts: internal strength and friction strength. The unconfined strength of brittle materials decreases after damage. Xi et al.[25] thought that, for pre-splitting specimens, when the stress was far less than the compressive strength of the rock, crack initiation and propagation would occur once or more.

Li et al.[26] analyzed the variation of elastic energy, fracture energy, and residual elastic energy in the whole process of rock compression and failure based on the stress−strain curve in the

Received: July 1, 2021
Accepted: September 10, 2021
Published: September 20, 2021

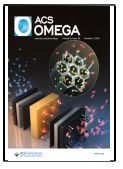

experiments. Wang et al.[13] thought that the elastic properties, failure strength, and failure mode of transversely isotropic shale were quite different between vertical and parallel bedding directions.

Because of the low homogeneity of shale, researchers at home and abroad pay little attention to crack initiation and propagation, and most of them focus on other rocks or rock-like materials.[27−31] Li et al.[24,32] studied the progressive fracture behavior of brittle lithologic rocks, such as shale and granite. Lajtai[33] divided the failure process of rock materials under uniaxial compression into six stages. Moreover, Arora and Mishra,[34] Liu et al.,[35] and Wang et al.[36] have conducted biaxial compression research on shale rocks, sandstone, and rock-like materials, respectively. Zhang et al.[37] studied the lithology of layered rock salt. Bobet and Einstein[38] studied the fracture behavior of gypsum specimens under uniaxial and biaxial compression and revealed the process of crack slip, wing-shaped crack initiation, secondary crack initiation, crack coalescence, and ultimate failure of the gypsum specimens under uniaxial and biaxial compression. Bobet[39] also studied the crack penetration of rock-like materials with two pre-existing fissures. Wong et al.[40] conducted an experimental analysis on the crack penetration of rock-like materials containing three cracks and put forward the "failure criterion" of two coalescence modes. Li et al.[41] used similar material models and numerical simulation methods to explore the mechanical properties and crack propagation behavior.

AE testing technology and CCD photography are effective observation methods for studying the crack/defect propagation in these kinds of brittle materials. At present, these two technologies are widely used to study the internal damage and fracture behavior of rock materials[25,42,43] Pan et al.[44] thought that acoustic emission counting could be used to characterize the damage and failure of specimens during compression, and the evolution process of the local stress field obtained by CCD could be used to analyze the coalescence of cracks in specimens. Jiang et al.[45] studied the acoustic emission characteristics of sandstone specimens under uniaxial cyclic loading and used RA and AF analysis methods to characterize the cracking mode with a few sensors. Ganne et al.[46] divided the cumulative acoustic emission activity into four stages, corresponding to the generation, propagation, penetration, and ultimate failure of microcracks. Huang et al.[47] established the relationship between the axial stress, acoustic emission count, and crack penetration process. Yang et al.[29] observed that the acoustic emission count of fractured specimens was more dispersed than that of intact specimens.

Zhang et al.,[48] Xi et al.,[25] and Mousavi Nezhad et al.[49] also used various numerical simulation software and methods to study crack propagation in heterogeneous rock mass, and the latter also proposed a model framework to simulate the initiation and propagation of pre-cracks. Other scholars[12,15,50] had also studied the crack growth and strength change of shale under other treatment conditions.

To study the deformation and failure process of shale and other rocks from meso- and macroperspectives, scholars at home and abroad began to use various new technologies and equipment to conduct experiments. Morris et al.[51] made new material specimens by using 3D printing technology and carried out uniaxial and biaxial tests using a CCD digital image system. Duan et al.[52] analyzed the evolution process of shale micropore structure distribution by X-ray microscopy and divided it into four stages: damage weakening, linearization, damage evolution and stable development, and damage-accelerated development. After that, Duan et al.,[53] based on real-time CT scanning technology, put forward that the pores have a negative influence on shale compressive strength and obtained the variation law of fracture volume under different stress levels. Zuo et al.[14] used scanning electron microscopy (SEM) to conduct a microscopic three-point bending test on Longmaxi shale specimens with different fissure angles. Kawakata et al.[54] used CT scan data to reconstruct 3D images of rock specimens and directly observed the shape and spatial distribution of microcracks. Li et al.[32] used a new X-ray microcomputed tomography (micro-CT) equipment to help study the progressive failure process.

The above-mentioned scholars have done a lot of research on non-layered specimens with the pre-existing fractures/fissures, while the exploratory study on brittle shale with natural fractures in this paper has a more prominent practical value. It is generally believed that the strength, deformability, and failure behavior of rock materials are strongly influenced by the widely distributed natural cracks.[55,56] For cylindrical (or square) specimens with a pre-existing fissure, different modes of crack propagation can be realized by changing the fissure angle of the pre-existing fissure so as to simulate the orientation of primary joints.

This investigation relied on photographic monitoring and the AE technique to obtain the real-time crack evolution process in the process of the whole deformation failure, which was not performed for the fissured shale rocks in previous studies. Thus, this paper aims to investigate the effect of fissure angle (α) on the strength characteristics, failure modes, and crack propagation process. First, shale specimens with a single-prefabricated fissure were processed and uniaxial compression tests were carried out. Simultaneously, acoustic events were recorded, and a CCD camera was used to characterize the crack propagation process. Second, we analyzed a real-time crack evolution process in fissured shale specimens under uniaxial compression on the basis of real-time CCD photographs and AE events. Moreover, the crack initiation angle and extension angle were calculated and analyzed, the relationship between the crack initiation stress, strength, and crack angle was compared, and the proportion of tensile and shear cracks at different stages of the whole compression process was briefly analyzed. Finally, the mechanical mechanism of crack evolution and perforation orientation was discussed.

2. SPECIMEN PROCESSING AND TEST PROCESS

2.1. Specimen Processing. All specimens in the test were taken from the black shale outcrops in the boundary of the Wufeng−Longmaxi shale gas field in the southwest margin of Sichuan Basin, and the rock specimens had clear bedding and good integrity. The elastic modulus, uniaxial compressive strength, and average density of the original intact shale specimens with horizontal bedding are 10.59 GPa, 174.32 MPa, and 2.55 g/cm^3, respectively.

According to the method proposed by ISRM,[57] the height-to-width ratio of the specimen should be in the range of 2.0−3.0 so as to reduce the influence of geometry on the test results. Therefore, all shale specimens in this test are square with a height of 100 mm, width of 50 mm, and thickness of 25 mm (aspect ratio of 2.0 and surface roughness within ±0.02 mm). The bedding direction of all specimens is horizontal and perpendicular to the loading direction in the uniaxial loading test. All specimens were stored in a dry environment at room

https://doi.org/10.1021/acsomega.1c03431
ACS Omega 2021, 6, 25461−25475

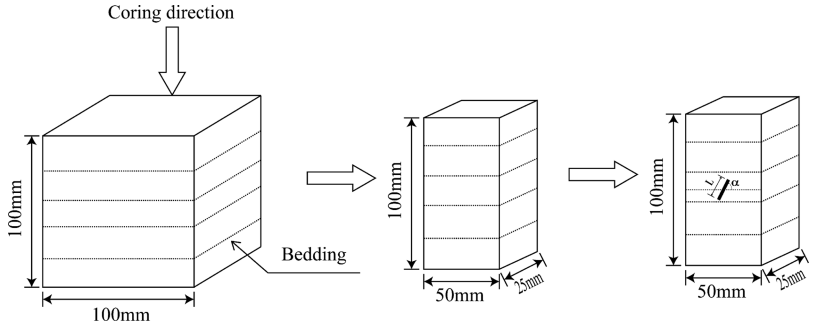

Figure 1. Machining process and related parameters of shale specimens.

Table 1. Geometric Parameters of Shale Specimens with a Prefabricated Fissure

fissure angle (°)	specimen	height (mm)	width (mm)	thickness (mm)	weight (g)	density (g/cm^3)
0	S-0-01	100.09	50.32	25.13	321.66	2.5414
	S-0-03	100.02	50.26	25.12	321.24	2.5439
30	S-30-01	100.33	50.23	25.36	322.43	2.5229
	S-30-02	100.08	50.18	25.34	321.22	2.5242
	S-30-03	99.91	50.2	25.16	321.45	2.5474
45	S-45-01	100.15	50.24	25.08	320.15	2.5370
	S-45-02	100.08	50.14	25.16	322.41	2.5537
	S-45-03	99.78	50.29	25.22	321.78	2.5427
60	S-60-01	100.4	49.18	25.35	318.78	2.5468
	S-60-02	100.42	49.2	25.74	319.14	2.5095
	S-60-03	100.03	49.32	25.42	318.05	2.5361
90	S-90-02	100.27	50.42	25.19	322.6	2.5332
	S-90-03	100.08	50.27	25.24	321.42	2.5312
average		100.13	50.02	25.27	320.95	2.5362
error		0.1868	0.4542	0.1768	1.4691	0.0120

temperature. According to the fissure parameters of sandstone specimens containing a pre-existing fissure prepared by Yang et al.,[29] the length of the prefabricated fissure is 12 mm, which is defined as L, and the width is about 2 mm.

Because the thickness of the specimen is 25 mm, the designed fissure size could not be processed by the cutting disk. If a high-pressure water jet is used to cut the fissure, then it is easy to cause the surface of the shale specimen to peel off, which may not meet the test requirements. Therefore, referring to the processing method of a pre-existing fissure by Yang et al.,[28,29] a pre-existing fissure of about 2 mm (representing natural defects such as joints and flaws in shale) is obtained.

The specific processing of the specimens is shown in Figure 1, and the information of the specimens is shown in Table 1.

Considering the processing cost of specimens, the specimens with a pre-existing fissure in this paper were selected from five classical fissure angles defined as α, which were 0, 30, 45, 60, and 90°. Finally, the specimens were subjected to surface speckle treatment. In a dry environment, a layer of white primer on the observation surface (100 mm × 50 mm) was evenly sprayed, then a layer of black paint was sprayed after the white paint is dried, and then this cycle was repeated 4 times. After that, the specimens were placed in a natural dry environment for 12−24 h.

2.2. Experimental Method. To explore the influence of α on the strength characteristics, crack initiation, crack propagation, and crack coalescence behavior of the fissured specimens under uniaxial compression, the whole loading process was monitored by a CCD camera and AE instrument. The flow chart of the test is shown in Figure 2.

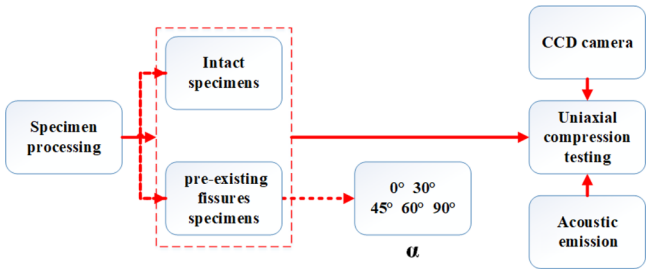

Figure 2. Flow chart of the experimental process.

The uniaxial compression test was carried out on an electronic precision material testing machine (Shimadzu Corporation, Japan, model AG-250Kn IS) in the State Key Laboratory of Coal Mine Disaster Dynamics and Control, Chongqing University. The maximum load capacity of the testing machine was 250 kN. The displacement control loading mode was adopted, and the loading rate was set at 0.1 mm/min. Before loading, Vaseline was pasted on both ends of the specimens to reduce the end friction. Furthermore, a pre-tightening force of 1 kN was applied so that both ends of the specimen could be in close contact with the indenter. The loading schematic diagram of the test is shown in Figure 3.

The AE instrument that adopted a 16CHS PCI-2 system was produced by PAC Company. The AE probe adopted Vaseline as a coupling agent, which was pasted on the observation surface of the specimens and near the prefabricated fissure and was tightly fixed with adhesive tape. The threshold of acoustic emission monitoring was set at 45 dB, and the acquisition frequency was 150 kHz.

https://doi.org/10.1021/acsomega.1c03431
ACS Omega 2021, 6, 25461−25475

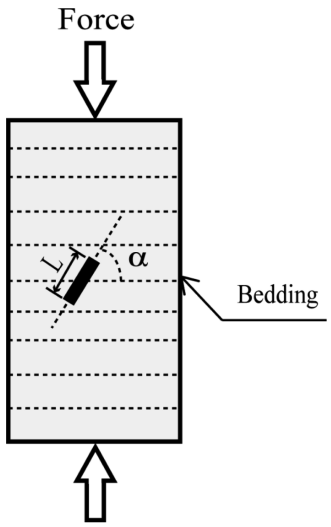

Figure 3. Loading diagram (α = 0, 30, 45, 60, and 90°).

In this study, a XCD-5005E CCD camera produced by Sony Corporation of Japan was used as the image monitoring equipment, the shooting resolution was set to 2448 × 2048, and the shooting speed was set to 1 FPS. The layout of the test system is shown in Figure 4.

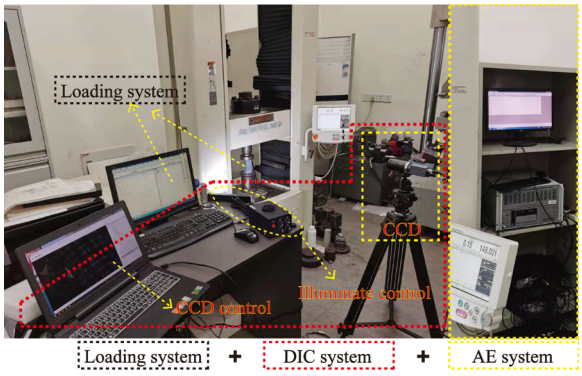

Figure 4. Layout of the test system.

3. STRENGTH CHARACTERISTICS ANSWER

3.1. Stress−Strain Curves. The representative curves of the axial stress−axial strain of the specimens under uniaxial compression tests are shown in Figure 5, and the maximum axial strain was less than 2%. The curves could be roughly divided into four stages: pore and fracture compaction, elastic deformation, crack initiation and propagation, and final failures.[32,33] The elastic deformation stage of the curves was flat, and the failure was sudden, which are typical brittle failure characteristics.

From the axial stress−strain curves, α had a predominant influence on the deformation and strength of fissured specimens. In the compaction stage, the curves were concave, and the process was very short. At this stage, the stress increase was low, and the curves of the fissured specimens at different fissure angles basically coincided, showing good consistency.

In the elastic deformation stage, the curves changed linearly with the increase in stress after the primary pores and fractures were closed. Compared with the fissured specimens with other fissure angles, the fissured specimens with α = 90° had the

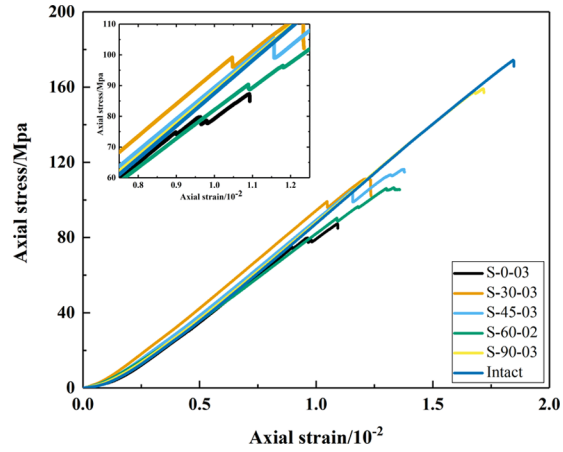

Figure 5. Stress−strain curves of the specimens with a prefabricated fissure.

longest elastic deformation stage. In addition, the slope of each specimen curve in the elastic stage was near consistent, and it was not affected by the change of α, which indicated that this batch of specimens had good consistency and small dispersion, and it was possible to approximately discuss the mechanical properties, failure modes, and crack propagation laws of shale specimens with different α values.

With the increase in loading force, the curves of the specimens with a prefabricated fissure deviated from the elastic stage, showing the significant nonlinear deformation. That is, there were many local "stress drop" areas, and the "drop" was accompanied by an audible sound in the test, but the corresponding curves of intact specimens did not cause this feature. Obviously, the formation of this area was related to the existence of the prefabricated fissure and the evolution of cracks including the prefabricated fissure. Detailed analysis will be carried out in combination with AE data and CCD photos, as shown in Section 5.1.

With the further increase in load, the curves reached its peak value and entered the final failure stage instantly. With a loud noise, the specimen finally failed and the test was stopped.

3.2. Mechanical Parameters of the Fissured Specimens. After the uniaxial compression test, various mechanical parameters varying with α were obtained, as shown in Figure 6. It could be seen that, with the increase in α, the uniaxial compressive strength (UCS) of the fissured specimens was positively changed. For the condition of α = 0°, the UCS of the specimen was the lowest with an average of 91.12 MPa. The UCS reached a maximum of 159.96 MPa, while α = 90°. For α = 30−60°, the UCS of the specimen had little difference, showing a slight fluctuation. On the whole, the UCS of the specimens enhanced with α increasing.

In addition, the peak strain and peak strength were positively correlated with the increase in α, and their local variation trends were similar. When α = 0°, the peak strain was the lowest, which was 1.19%. When α = 90°, the maximum peak strain reached 1.77%. When α = 30−60°, the peak strain was around 1.32%, with little change among them. The above analysis showed that the existence of a pre-existing fissure greatly weakened the UCS and corresponding peak strain of the shale specimen.

The elastic modulus E is defined as the slope of an approximate linear part in the stress−strain curve, and the deformation modulus E_{50} refers to the ratio of stress to the

https://doi.org/10.1021/acsomega.1c03431
ACS Omega 2021, 6, 25461−25475

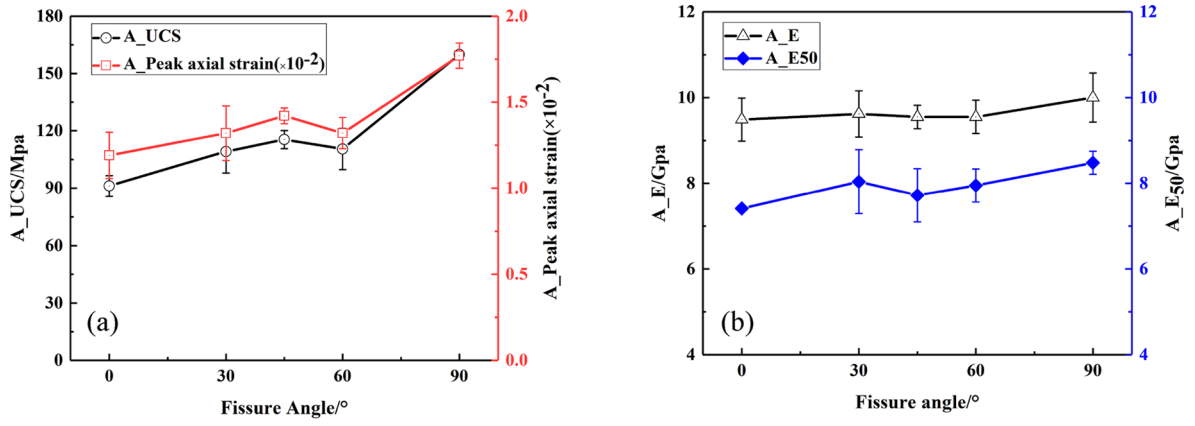

Figure 6. Mechanical parameters of shale specimens under uniaxial compression. (a) UCS and peak strain. (b) Elastic modulus and deformation modulus.

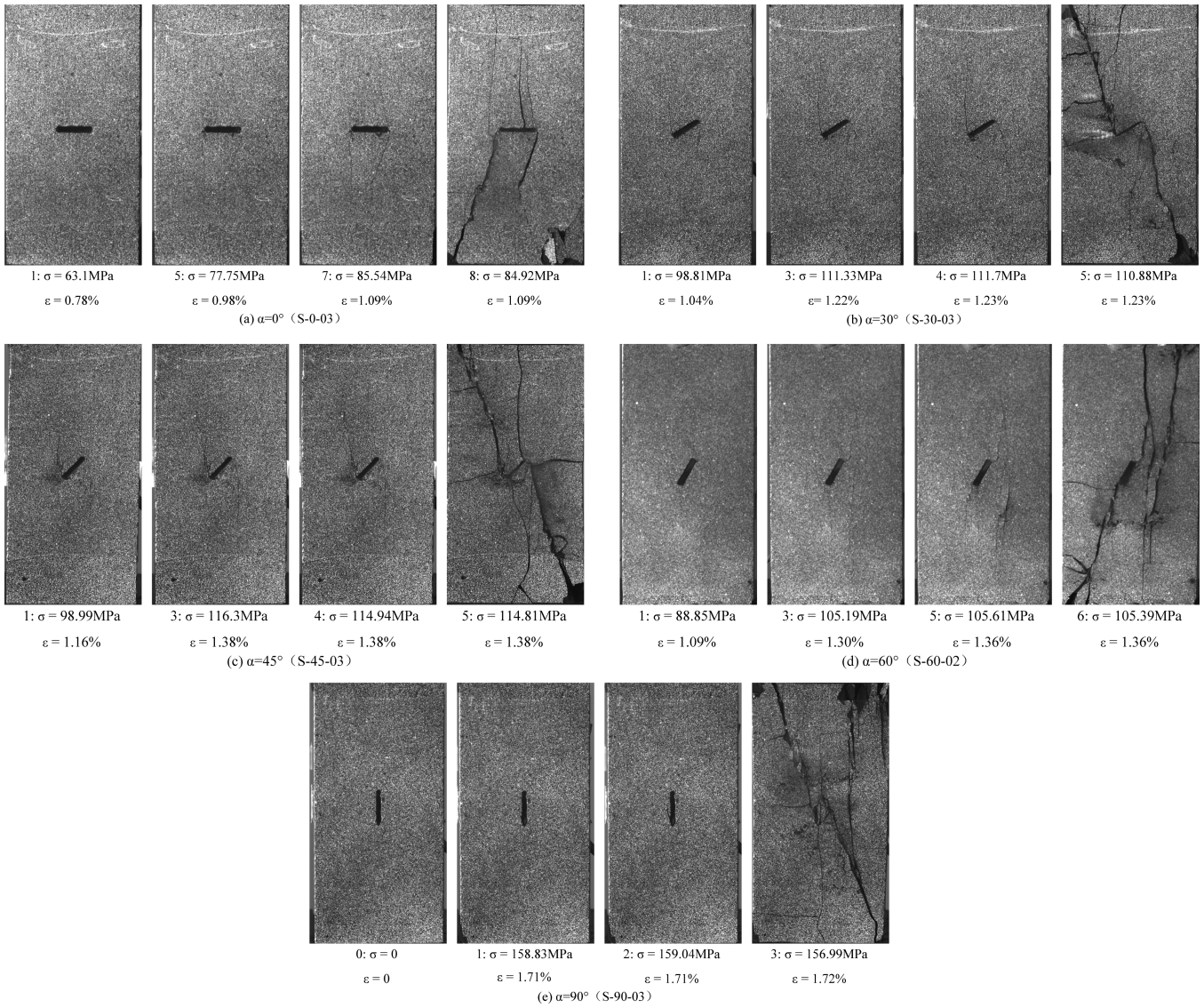

Figure 7. Crack evolution process of the fissured specimens during the whole deformation failure with respect to different fissure angles (0–90°). Note: The integers (0, 1, 2, 3, 4,...) below each small picture represent the time when cracks or surface spalling appear in each specimen. σ and ε, respectively, represent the stress and strain values at this moment.

corresponding strain at half the peak strength. Generally speaking, the deformation modulus E of a rock is much larger than that of rocks (E_{50} is generally used). The elastic modulus E represents the deformation resistance of the specimen when

https://doi.org/10.1021/acsomega.1c03431
ACS Omega 2021, 6, 25461−25475

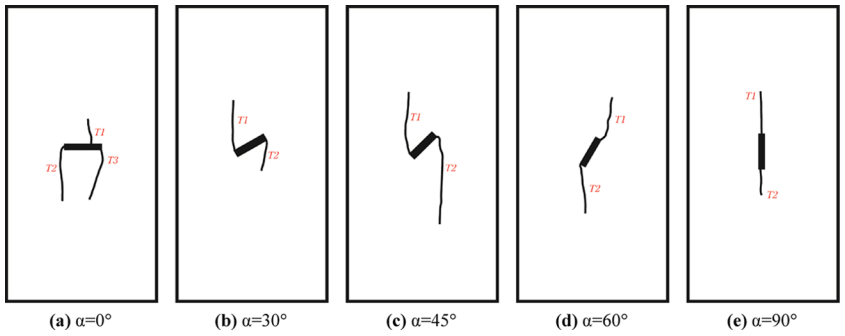

Figure 8. (a−e) Morphology sketch of initial crack distribution (T is the tension model).

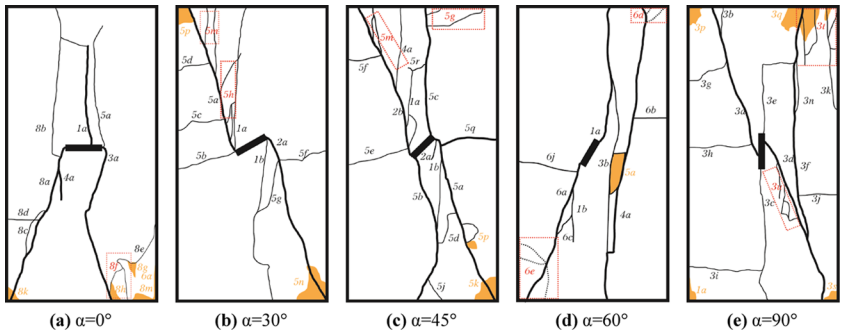

Figure 9. (a−e) Morphology sketch of the final crack distribution. Note: The number in the "numbers + letters" is the time of the crack occurrence, the letter is the crack appearing at this time, the red dotted box is the secondary crack clusters, and the yellow area is the spalling area.

it reaches the elastic stage after the compaction stage. Furthermore, the deformation modulus E_{50} includes the average deformation capacity of rocks including the compaction and elastic stage. Therefore, in this paper, we use two moduli: the elastic modulus E and deformation modulus E_{50}. The mechanical properties and deformation characteristics of fissured specimens are described and explained together. The former focuses on its elastic properties, while the latter focuses on the average deformability of fissured specimens, which could be obtained by analyzing the axial stress−strain curve, as shown in Figure 6b, with the increase in α, E, and E_{50} of the fissured specimens generally showing a slightly increasing trend. Obviously, various α values have little influence on E of the fissured specimens, but the damage and deformation resistance are still affected by the prefabricated fissure with varying α.

In a word, the influence of a pre-existing fissure on the UCS and peak axial strain of the specimens was far greater than that on E and E_{50}. The existence of the fissure weakened the UCS, which varied greatly under various α values, and the maximum UCS was at 90°.

4. CRACK MORPHOLOGY

In this uniaxial compression test, the CCD camera was used to monitor the whole deformation and failure process in real time. According to the phenomenon of crack initiation, propagation, and penetration and by screening all CCD pictures, the crack propagation process of the specimens with the prefabricated fissure was obtained, as shown in Figure 7.

4.1. Crack Distribution of the Fissured Specimens. Only four morphologies with significant changes were selected for arrangement, as shown in Figure 7. In addition, according to the photos (taken by the CCD camera) of the specimens with the prefabricated fissure before and after ultimate failure under uniaxial compression, the sketch map of initial crack distribution and the sketch map of crack distribution after final failure were drawn, as shown in Figures 8 and 9, respectively. The following contents present a detailed analysis on the influence of the pre-existing fissure and α on the crack evolution.

The crack initiation point refers to the failure point initiated from the tip of the pre-existing fissure. It can be seen from Figure 8 that the crack initiation points of the fissured specimens with various α values were located at the tip of the prefabricated fissure. It should be noted that there were initial cracks at the tip and side of the prefabricated fissure for $\alpha = 0°$.

According to the CCD photos in Figure 8, the propagation paths of cracks were different in the initial stage of cracking when α ranged from 0 to 90°. The cracking process was influenced by the internal structure, primary bedding or defects, in situ stress state, and other factors.[12,13,41,46,47] The initial cracks started from the tip of the precast fissure expanding along the main stress direction and directly passing through the weak bedding planes longitudinally but did not turn to the horizontal bedding planes, which was because the stress concentration always existed at the tip of the pre-existing fissure at the initial stage of cracking, and it advanced with the crack propagation at the pre-existing fissure tip. In addition, on the one hand, under the action of axial load, the cracks searched the weakness direction and broke through along the principal stress direction under the action of axial load. On the other hand, the maximum principal stress inhibited the initiation and development of cracks in the direction perpendicular to the stress. That is, it inhibited the transverse extension of cracks to form horizontal cracks in this period.[58] This is basically consistent with Xin et al.'s description and explanation of stress concentration and failure around a single fracture.[59]

https://doi.org/10.1021/acsomega.1c03431
ACS Omega 2021, 6, 25461−25475

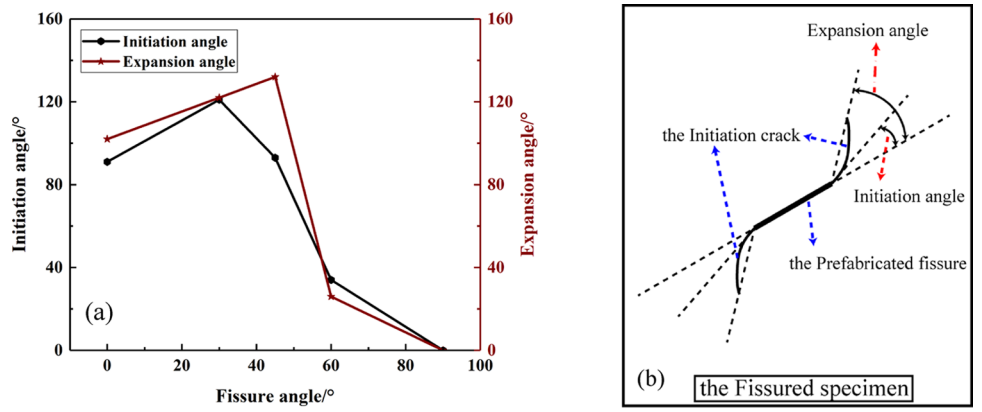

Figure 10. (a) Initiation angle and the expansion angle and (b) measuring method of the angles. Note: The crack initiation angle at the tip of the prefabricated crack is the angle between the crack initiation point at the tip and the extension direction of the prefabricated crack; the expansion angle at the tip of the prefabricated crack is the angle formed by connecting a line between the breakthrough point and the starting point to the extension direction of the prefabricated crack after the initial crack develops further. Both are the semi-quantitative representations.

Combined with Figure 8, the cracks initiated in the form of tensile cracks from the tip of the prefabricated fissure for α = 0−90°. The initial cracks of the fissured specimens were three tensile wing cracks for α = 0°. For α = 30−45°, the initial cracks were all anti-tensile cracks. For α = 90°, the initial cracks included two vertical tensile cracks.

To further analyze the crack initiation, according to the results recorded by the CCD camera, the crack initiation angle and the expansion angle of the initial cracks at the tip of the prefabricated fissure were obtained by using Image-J Software v1.8.0 (National Institutions of Health, USA),[60] and the measuring results and measuring methods are shown in Figure 10. It was worth explaining that the initiation angle represents the initiation orientation of the initiation point, while the expansion angle represents the further extension orientation of it after the initial cracks were produced.

It can be seen from Figure 10b that the crack initiation point deviated from the tip of the pre-existing fissure for the fissured specimens. For α = 0°, both the initiation angle and the expansion angle were near 90°. For α = 30°, the initiation angle was the maximum. The initiation angle decreased rapidly with α increasing, while α = 30−90°. With the further increase in loading force, the cracks expanded further after crack initiation. Except for α = 45°, the variation of the extension angle and the initiation angle with α values was basically consistent, which was similar to the relationship in Brazil splitting tests conducted and observed by Wang et al.[61] With α increasing, the initiation angle and the expansion angle first increased and then decreased. It showed that, during the process from the crack initiation to propagation, the crack propagation trajectory was affected by the initiation angle and nearly expanded along this angle. In addition, for α = 30−45°, the initiation angle and the expansion angle were both at a high level. This was due to the formation of reverse tensile wing cracks at these angles, which had a great influence on the ultimate failure modes.

4.2. Ultimate Failure Modes. Three failure types had been observed in the uniaxial compression tests of shale specimens: tensile failure, shear failure, and mixed tensile-shear failure.[50] According to the characteristics of cracks, the failure modes of rocks could be determined.[32] To observe the crack morphology more intuitively, the data shown in Figure 7 was binarized by MATLAB R2018b software,[62] and the surface spalling near both ends of the specimen was locally optimized to obtain, as shown in Figure 11. According to the classification method of failure modes by Wang et al.,[28,29,61] the failure

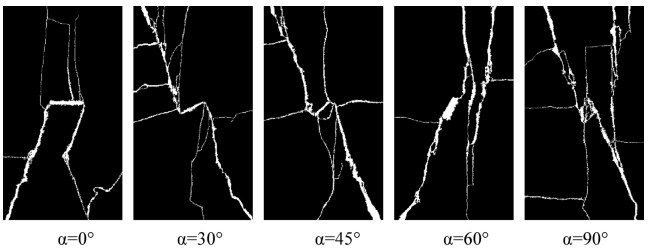

Figure 11. Ultimate failure modes of the fissured specimens treated by binarization.

modes of the specimens with the prefabricated fissure were classified into the following categories: shear slip at the fissure tip (I), tensile failure at the tip (II), mixed tensile-shear failure at the tip (III), tensile failure along the bedding near the tip (IV), tensile-shear failure along the bedding (V), and tensile failure in the middle of the specimen along the vertical direction (VI).

From Table 2, it could be seen that shale specimens receive the combined action of the horizontal bedding and the pre-existing fissure, and the failure modes of the fissured specimens were the combination of multiple failure modes, with shear cracks and tensile cracks as the main crack forms. Combined with Figure 11, the failure modes of specimens with the prefabricated fissure included shear slip (I) and mixed tensile-shear failure along the bedding (V). There were clear differences in crack characteristics and failure modes of the fissured specimens with α values changing.

Table 2. Ultimate Failure Modes of the Specimens with a Prefabricated Fissure

	types of failure modes					
fissure angle (°)	I	II	III	IV	V	VI
0	√		√		√	√
30	√	√	√	√	√	
45	√	√	√	√	√	
60	√		√	√	√	
90	√	√	√	√	√	

https://doi.org/10.1021/acsomega.1c03431
ACS Omega 2021, 6, 25461−25475

Among all the failure modes of the fissured specimens with the prefabricated fissure, there were not only main cracks that cut through the bedding vertically and main cracks extending transversely along the bedding but also main cracks that penetrated bedding obliquely and other secondary cracks. The ultimate failure modes of the fissured specimens were mixed tensile-shear failure. This was similar to the conclusion of Li et al.[32] on the failure modes of shale under uniaxial compression where the failure mechanism of shale with the horizontal bedding under uniaxial compression was mainly tension failure or comprehensive tension-shear failure.

According to Figure 11, it was obvious that the main cracks were generated around the prefabricated fissure. Combined with the crack geometry and propagation mechanism, there were many kinds of crack failure modes: tensile crack, shear crack, mixed tensile-shear crack, transverse crack, and surface spalling, as shown in Table 3. For the fissured specimens, most

Table 3. Crack Types of the Intact and Fissured Specimens

		types of cracks				
fissure angle (°)	crack development process	tensile	lateral	mixed tensile-shear	shear	spalling
intact	initial stage					√
	failure stage	√	√	√	√	√
0	initial stage	√				
	failure stage	√	√	√	√	√
30	initial stage	√				
	failure stage	√	√	√	√	√
45	initial stage	√		√		
	failure stage	√	√	√	√	√
60	initial stage	√		√		
	failure stage	√	√	√	√	√
90	initial stage	√				
	failure stage	√	√	√	√	√

of the secondary cracks in the horizontal direction were mixed with oblique tension-shear to form total penetrating networks, as shown in Figure 11.

By comparing the ultimate failure modes of the fissured specimens with different fissure angles, it was found that, for α = 30−45°, two main cracks penetrated through the prefabricated fissure and the loading end face and one main crack penetrated through the horizontal bedding that emerged at the tip of the prefabricated fissure. The former realized mutual penetration, many secondary crack clusters were formed laterally of the shear-slip main cracks, and the communication between natural joints and horizontal bedding was realized. Finally, a crack network composed of natural joints, horizontal bedding, and the prefabricated fissure was formed. For α = 0 and 60−90°, there were no more connections between the main cracks formed around the pre-existing fissure, and there were few secondary crack clusters around the main cracks. The overall fracture network was sparse. Therefore, it could be considered that the prefabricated fissure for α = 30−45° played an obvious role in forming a large-area crack network.

5. AE CHARACTERISTICS

Acoustic emission events referred to the deformation and failure of the fissured specimens under load, accompanied by a large number of microcracks, which lead to the release of stored energy in the specimens.[63] Monitoring the AE signal combined with CCD photos of the fissured specimens was helpful for analyzing the whole process of crack initiation, propagation, and penetration under uniaxial compression.

5.1. AE Behaviors. Figure 12 shows the AE events of the fissured specimens with respect to different α values. The crack evolution and final crack distribution of the fissured specimens are shown in Figures 7 and 9, respectively. The numbers (integer 0, 1, 2...) shown in Figures 12 and 9 correspond to the sequence of cracking shown in Figure 7, and the yellow shading in Figure 9 represents surface spalling.

When the specimen with α = 0° was first loaded to stage 1 (ε = 0.78%, σ = 63.1 MPa), tensile crack 1a initiated at the point on the side of the prefabricated fissure. At stage 2 (ε = 0.90%, σ = 74.14 MPa), tensile crack 1a extended further with an obvious stress drop and AE counts. At stage 3 (ε = 0.96%, σ = 79.56 MPa), crack 3a initiated from the right-hand end of the prefabricated fissure with some AE counts. At stage 4 (ε = 0.96%, σ = 78.64 MPa), crack 4a initiated from the left-hand end of the prefabricated fissure with an obvious stress drop and AE counts. At stage 5 (ε = 0.98%, σ = 77.75 MPa), crack 5a initiated from the right-hand end of the prefabricated fissure with an obvious stress drop and AE counts. At the peak point of stage 6 (ε = 1.09%, σ = 87.24 MPa), more powder of shale rocks suddenly appeared in the prefabricated fissure and the width of the fissure increased obviously. Surface spalling 6a was observed below the right-hand corner of the specimen. At stage 7 (ε = 1.09%, σ = 85.54 MPa), the width of the pre-existing fissure continued to increase. Finally, at stage 8 (ε = 1.09%, σ = 84.92 MPa), the instability failure of the specimen occurred with the initiation and propagation of cracks 8a, 8b, 8c, 8d, 8e, and 8f. With the largest AE events and stress drop, surface spalling (8m, 8h, 8g, and 8k) was observed.

For the specimen with α = 30°, at stage 1 (ε = 1.04%, σ = 98.81 MPa), tensile cracks 1a and 1b initiated from the right-hand and left-hand end point of the prefabricated fissure, respectively, with an obvious stress drop and obvious AE counts. When the specimen was further loaded at stage 2 (ε = 1.21%, σ = 110.75 MPa), tensile crack 2a emerged at the left-hand end of the prefabricated fissure, and crack 1a extended further straightly with a slight stress drop and obvious AE counts. At stage 3 (ε = 1.22%, σ = 111.33 MPa), some shale powder appeared in the prefabricated fissure, and tensile cracks 1a and 2a extended further with a slight stress drop and obvious AE counts. At stage 4 (ε = 1.23%, σ = 111.7 MPa), crack 2a directly expanded. Finally, at failure stage 5 (ε = 1.23%, σ = 110.88 MPa), cracks 5a, 5b, 5c, 5d, 5g, 5h, 5f, and 5m, accompanied by a large AE event, were observed, as was surface spalling (5p and 5n).

For the specimen with α = 45°, at stage 1 (ε = 1.16%, σ = 98.99 MPa), tensile cracks 1a and 1b initiated from the two ends of the prefabricated fissure, respectively, with a large stress drop and obvious AE counts. With an obvious stress drop and AE event, cracks 2a and 2b initiated from the two ends of the prefabricated fissure at stage 2 (ε = 1.32%, σ = 113.22 MPa). At stage 3 (ε = 1.38%, σ = 116.3 MPa), crack 2b had a propagation suddenly with a little stress drop and AE event; at stage 4 (ε = 1.38%, σ = 114.94 MPa), cracks 1b and 2b had propagation, and crack 4a emerged suddenly with a little stress drop and AE events. With the initiation and propagation of cracks 5a, 5b, 5c, 5d, 5e, 5f, 5g, 5j, 5q, 5r, and 5m, instability failure of the specimen occurred at stage 5 (ε =

https://doi.org/10.1021/acsomega.1c03431
ACS Omega 2021, 6, 25461−25475

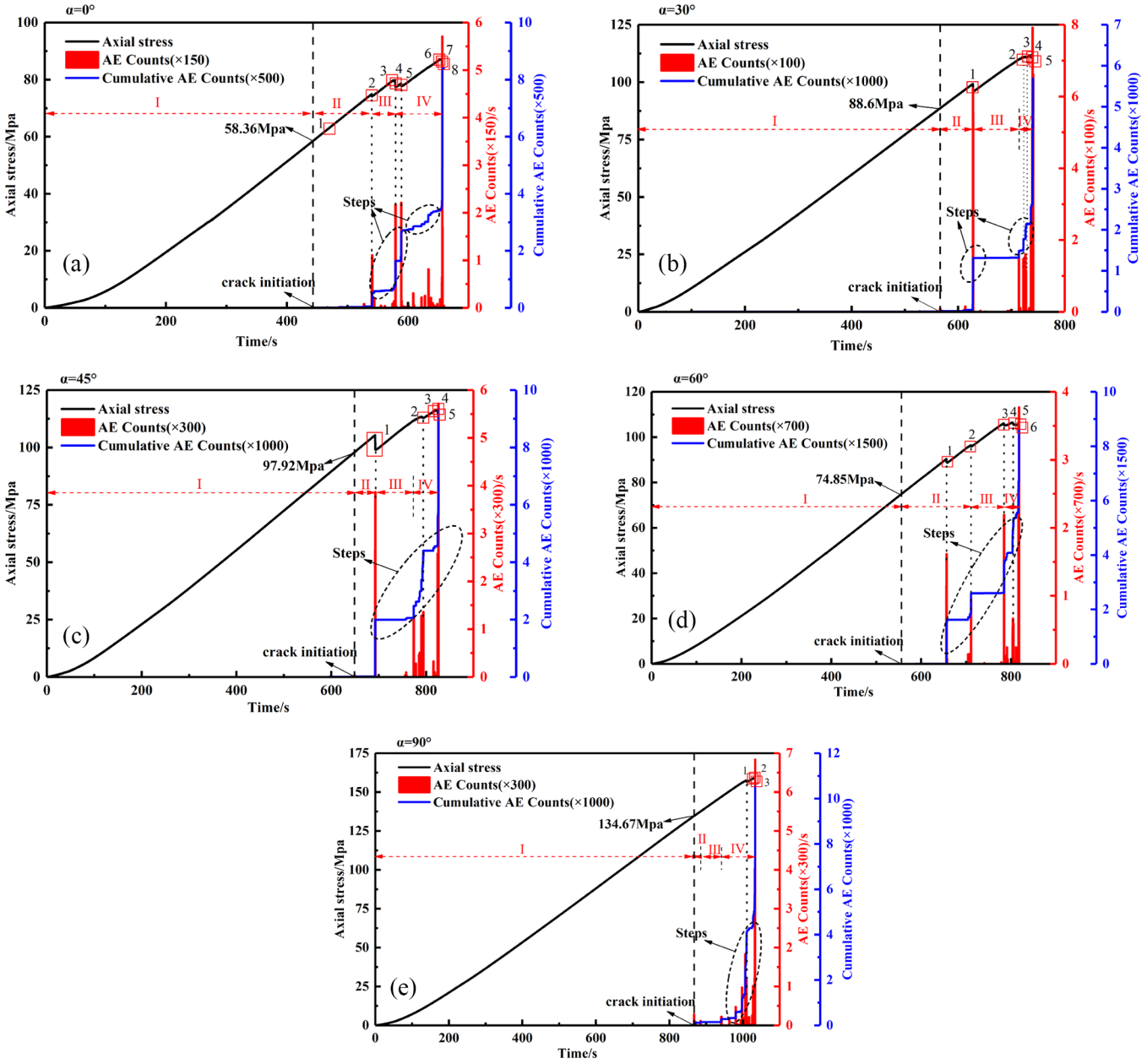

Figure 12. Relationship between axial stress, AE counts, and accumulated AE counts. (a) 0, (b) 30, (c) 45, (d) 60, and (e) 90°. Note: The integers (1, 2, 3, 4,...) on the stress-time curve represent the time when cracks or surface spalling appear in each specimen and correspond to the numbers (1, 2, 3, 4,...) in Figures 7 and 9.

1.38%, σ = 114.81 MPa), accompanied by a large AE event, was observed, as was surface spalling (5k and 5p).

For the specimen with α = 60°, at stage 1 (ε = 1.09%, σ = 88.85 MPa), tensile cracks 1a and 1b initiated at the two ends of the prefabricated fissure with an obvious stress drop and obvious AE counts. At stage 2 (ε = 1.18%, σ = 96.26 MPa), cracks 1a and 1b propagated further with a little stress drop and obvious AE counts. At stage 3 (ε = 1.30%, σ = 105.19 MPa), on the right side of the prefabricated fissure, with an obvious stress drop and obvious AE counts, a nearly vertical crack 3b emerged instantly. At stage 4 (ε = 1.33%, σ = 106.27 MPa), on the right side of crack 3b, crack 4a occurred with an AE event. At stage 5 (ε = 1.36%, σ = 105.61 MPa), surface spalling (5a) emerged among cracks 3b and 4a with a slight AE event. Finally, failure stage 6 (ε = 1.36%, σ = 105.39 MPa) was reached, and the occurrences of cracks 6a, 6b, 6c, 6d, 6e, and 6j caused an obvious AE event.

For the condition of α = 90°, at stage 1 (ε = 1.71%, σ = 158.83 MPa), surface spalling 1a occurred below the left-hand corner of the specimen with an obvious AE event, accompanied by some small particles emerging in the prefabricated fissure. At stage 2 (ε = 1.71%, σ = 159.04 MPa), some small particles spall from the prefabricated fissure with some AE counts. At stage 3 (ε = 1.72%, σ = 156.99 MPa), tensile cracks 3c and 3e initiated and propagated from the two ends of the prefabricated fissure, and cracks 3a and 3d initiated from the two sides of the prefabricated fissure. Moreover, a large AE event was observed accompanied with the initiation and propagation of the all cracks and surface spalling.

5.2. Four Stages of AE Events. To explore the relationship between axial stress, AE events, and crack

https://doi.org/10.1021/acsomega.1c03431
ACS Omega 2021, 6, 25461−25475

evolution of the fissured specimens under uniaxial compression with loading time, the result in Figure 12 is obtained. The result shows that the stress drop on the axial stress-time curve was in good agreement with the sudden change of AE counts, and the accumulative AE count-time curve would form a step at the same time. The greater the stress drop amplitude, the higher the "step" in the cumulative AE count-time curve.

According to the AE signals of the fissured sandstone specimens under uniaxial compression, Yang and Jing[28] divided the whole loading process into two periods: the quiet period and active period. Lu et al.[50] divided the loading process into two stages according to the AE signals of shale Brazil split specimens and took the AE signals of crack initiation as the critical point. Therefore, according to the AE characteristics of the fissured specimens, the whole AE period was divided into four typical stages: the initial quiet period (I), active period (II), silent period before failure (III), and failure period (IV).

In the initial quiet period (period I), the AE counts were few and sparse, the cumulative AE-time curves basically coincided with the time axis, and there was no formation of macroscopic cracks at the pre-existing fissure. This stage took a long time, and the AE signal had nothing to do with the fissure angles of the prefabricated fissure.

As the loading increased, the events of the crack initiation were monitored, so the crack initiation stress could be obtained from the stress-time curves. Subsequently, the AE events entered into the active period (period II). In this period, AE events were generated sporadically, and the AE counts were very few, which was due to the weak AE signals caused by microcrack initiation. However, the energy stored in the specimens continued to accumulate, and the first stress drop appeared in the stress-time curves. Immediately after the release of energy, a large number of AE counts appeared, and the active period ended. At that moment, there was a macroscopic crack initiation at the tip of the pre-existing fissure of the fissured specimens (for example, at time 2 in Figure 12a and at time 1 in Figure 12b−e).

After entering the silent period before failure (period III), because the energy had been released after the first stress drop, the generated macrocracks waited for new energies to gather, and the generation of macrocracks weakened the propagation of AE signals, resulting in the decrease in AE signals. Then, accumulative AE-time curves remained horizontal and the AE signals entered the failure period (period IV).

After the AE signals entered the failure period (period IV), the AE signals were dense, the cumulative AE-time curve was in the ascending stage, and the corresponding rising steps were concentrated until the specimen was finally destroyed. At this time, the strongest AE event was generated, which showed that the AE counts were the largest.

For the fissured specimens with $\alpha = 0°$, AE events were not very active and had a few AE counts, except for a few large AE counts. For $\alpha = 90°$, the AE behavior remains active in stages II, III, and IV, and the AE counts are dense but low, except for the sudden increase in some AE counts.

Combining with the above analysis of crack growth and AE characteristics, we can get the following points.

For the fissured specimen of $\alpha = 0°$, the tensile crack begins at the side of the prefabricated fissure. For $\alpha = 30–90°$, tensile cracks start from the two ends of the prefabricated fissure. At the same time, for $\alpha = 90°$, shear cracks appeared on both sides of the prefabricated fissure. With the increase in α values, corresponding crack initiation stress and AE counts increased. By analyzing the cumulative AE curves of fissured specimens, it could be found that, when α was 60°, the steps are the most, and the length and height of the steps are average and consistent. The cumulative AE curves with $\alpha = 30$ and 45° were similar, and both contained two steps with similar shapes, which corresponded to the expression of failure modes when $\alpha = 30$ and 45° in Section 4. When $\alpha = 60°$, there were three obvious stress drops in AE events at times 1, 2, and 3, and the heights of steps formed in the cumulative AE curves were almost the same. The AE event-fissured specimens were more concentrated in the failure period (period IV) when $\alpha = 90°$, the cumulative AE curve was also extremely steep, and the only significant ascending step appeared near the peak stress. Before that, the curve had been flat, which was consistent with the crack evolution process of the specimen. The cumulative AE curve showed a "multistep", which indicated that the energy of brittle shale was accumulated and released continuously under the continuous load. The formation of this "step" corresponded to crack propagation and secondary crack germination. In addition, the maximum stress drop occurred in the failure period (period IV). When $\alpha = 30–45$ and 90°, the time (period II + period III + period IV) from crack initiation to final failure was shorter than when $\alpha = 0$ and 60°.

5.3. Crack Initiation Stress. According to the characteristics of AE events, an inflection point appears in the middle of the cumulative AE curve. Before the inflection point, AE events remain silent, and after this, AE events begin to increase, which makes the curve have an upward trend. Therefore, the stress value corresponding to the point can be used as the threshold of crack initiation of the shale rock, that is, crack initiation stress.

According to the AE events of the fissured specimens obtained, the crack initiation stress is acquired and shown in Figure 13. It can be found that the crack initiation stress

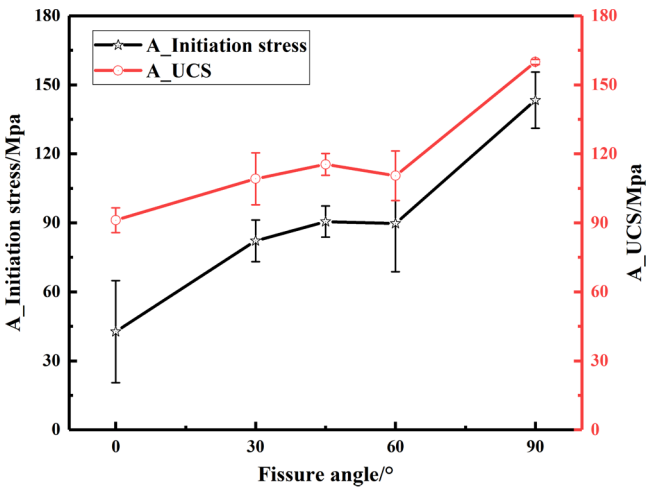

Figure 13. Crack initiation stress and UCS of the fissured specimens.

increases with the increased fissure angle ($\alpha \neq 60°$). Combined with Figure 6a, it can be found that the relationship between the initiation stress, UCS, and peak strain with the α values was basically consistent, showing an overall positive correlation. Especially, for $\alpha = 60°$, the initiation stress drops the same as the corresponding UCS and peak strain. This was because the pre-existing fissure of $\alpha = 60°$ formed a dominant angle of 30°

https://doi.org/10.1021/acsomega.1c03431
ACS Omega 2021, 6, 25461−25475

with the loading direction and a weak plane, creating rock failure.

5.4. Influence of the Fissure Angle on Hydraulic Fracturing. For the AE signals, the distribution of AF (AE count/duration) and RA (rising time/amplitude) was often used to further analyze the rock failure modes.[45,50] The proportion of tensile and shear cracks in the total loading process and the post-peak loading stage was obtained, as shown in Table 4. The RA-AF distribution of the specimens with different fissure angles was also drawn (Figures 14 and 15), according to the average values in Table 4.

Table 4. Proportion of Different Cracks in Various Loading Periods

condition	the proportion of different cracks in various periods (%)			
loading period	total loading process		the loading process after peak stress	
fissure angle (°)	tensile	shear	tensile	shear
0	83.9	16.1	61.2	38.8
30	83.1	16.9	67.1	32.9
45	83.5	16.5	71.9	28.1
60	89.5	10.5	88	12
90	83.5	16.5	77.7	22.3

According to Table 4, tensile cracks were the main form of the fissured specimens for $\alpha = 0-90°$ during the whole loading process. Except for $\alpha = 60°$, the tensile and shear cracks produced by the fissured specimens with other α values are 83.1−83.9 and 16.1−16.9%; obviously, the divergence is light. On the post-peak loading stage, except for $\alpha = 60°$, likewise, the proportion of tensile cracks is still high (61.2−77.7%) but decreases greatly and the proportion of shear cracks increases hugely, ranging from 22.3 to 38.8% compared with the proportion in the whole loading period.

Combined with Figure 15, it could be seen that, on the post-peak loading stage, the initiation and propagation of shear cracks were greatly increased and the possibility of shear failure was intensified, which was consistent with the mixed tensile-shear failure modes of the specimen with a pre-existing fissure.

6. DISCUSSION

6.1. Cracking Evolution and Its Mechanical Mechanism. In this paper, the uniaxial compression test of prefabricated shale specimens is carried out. According to the stress−strain curves of brittle rocks obtained by the test, the deformation failure process of brittle rocks can be divided into five stages, namely, crack closure, linear elastic deformation, crack initiation and stable crack growth, crack damage and unstable crack growth, and failure and post peak behavior.[64]

However, in this test, the stress−strain curve of fissured specimens with horizontal bedding has no post-peak stage, and the compaction stage is short. Therefore, the failure process of the fissured specimens is divided into four parts: crack closure and linear elastic deformation, crack initiation and stable crack growth, crack damage and unstable crack growth, and failure and around peak behavior. These four stages correspond to the four periods divided in this paper: initial quiet period (I), active period (II), silent period before failure (III), and failure period (IV).

In the test, when the vertical load reaches the crack initiation stress value, the tensile crack first starts at or near the prefabricated fissure end. This shows that the prefabricated fissure guides the crack initiation.[65] In addition, at the moment when the initial crack emerges at the end of the prefabricated fissure of shale specimens, the initial crack will extend a very short distance to the extension direction of the prefabricated fissure. However, this tiny distance is fleeting, and then it deviates upward or downward. This is due to the stress concentration at the prefabricated fissure ends before crack initiation. In the tiny range of the end, the stress concentration can be regarded as evenly distributed around the end. Under the action of load, the breakthrough is found, and a tiny crack is produced finally. With the load increasing, the tensile crack at the end of the prefabricated fissure extends further, accompanied by the generation of a secondary crack. These cracks eventually propagate in the loading direction, and the crack initiation angle is almost the same as the extension angle. This is because the crack propagation is mainly dominated by the initial crack direction and propagates along the maximum principal stress direction.[65,66]

According to Griffith's microstrength theory, under the action of external stress, stress concentration occurs and begins to expand first at the crack tip, then the cracks collude with each other, and finally, macro failure is formed.[20] It is worth noting that, in the final failure modes of the fissured specimens, cracks along the horizontal bedding occurred. This is because, for layered rocks, the bedding plane belongs to the geological weak plane, there are a large number of primary microcracks near the bedding plane, and the cementation strength between horizontal bedding is weak, which makes it easier to reach the limit stress state.[61] Before the failure of the specimen, the horizontal bedding was perpendicular to the maximum principal stress, and there was no crack along the horizontal bedding. However, the stress that is not perpendicular to the bedding plane in the end exceeds the local maximum failure strength, and then mixed tension-shear cracks caused by failure along the bedding plane or cutting through the bedding at low angles are produced. In addition, the integrity of local mineral bundles is damaged due to the existence of the prefabricated fissure. From the vertical direction, the projection of the fissure length on the horizontal direction shows that the larger the crack angle, the smaller the projection length. The smaller the failure degree of the mineral beam, the smaller the strength of the fissured specimen when weakened. This further explains the strength characteristics of the fissured specimen with different fissure angles in this paper.

To sum up, evolution occurred through a process involving the coalescence of smaller cracks into larger cracks, which in turn coalesced until a critical plane of failure was formed.[64]

6.2. Selection of Perforation Orientation for Fracturing Horizontal Wells. With the advancement of technology and the continuous updating of fracturing equipment, fracturing technology at the horizontal well has developed from staged fracturing and multistaged fracturing to large-scale staged multicluster volume fracturing.[67] As an important part of horizontal fracturing, perforation not only is related to the production of oil and gas wells but also has a significant impact on the subsequent stimulation measures. In this test, the original joints are simulated by setting the prefabricated fissure with various fissure angles in shale gas reservoirs with horizontal bedding. Combined with the previous analysis of crack evolution and final failure modes of the fissured

https://doi.org/10.1021/acsomega.1c03431
ACS Omega 2021, 6, 25461−25475

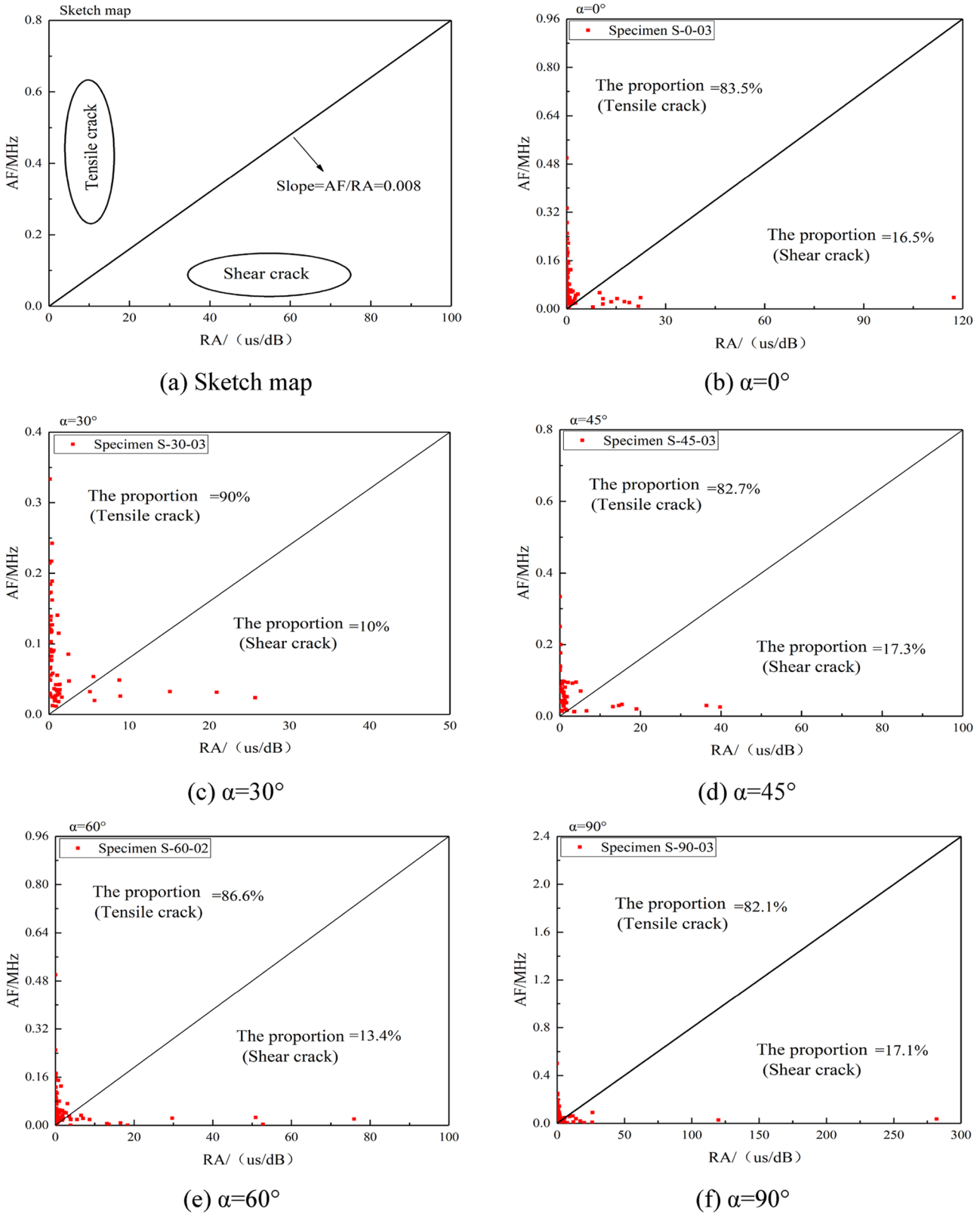

Figure 14. (a–f) RA-AF distribution of the fissured specimens with different fissure angles. Note: The diagonal slope of all patterns is 0.008 (slope = AF/RA = 0.008).

specimens (Section 4.1), the fissured specimens have the most cracks around the prefabricated fissure for α = 30 and 45°. The fissure angles of 30 and 45° play an obvious role in forming a large-area crack network and secondary crack clusters surrounding the multiple main cracks, thus bringing about the perfect penetration of natural joints, bedding, and artificial fissure. Furthermore, the rock network is formed around the prefabricated fissure. As a result, the crack degree of the rock

https://doi.org/10.1021/acsomega.1c03431
ACS Omega 2021, 6, 25461−25475

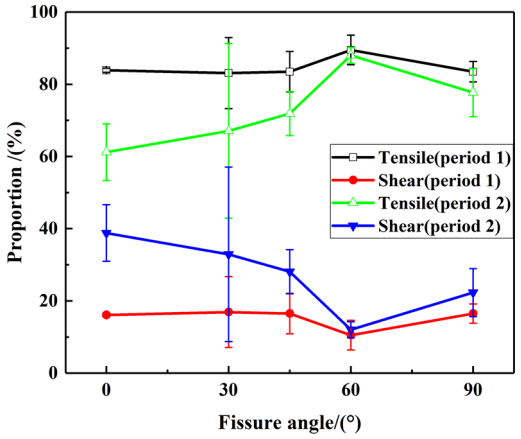

Figure 15. Proportion of different cracks of shale specimens with various fissure angles in various loading periods.

mass around the prefabricated fissure and the whole specimen is larger. For the fissured specimens of α = 0, 60, and 90°, the existence of the prefabricated fissure promotes the local crack network, and the final failure mode is closer to the vertical split failure. When α = 30 and 45°, the crack initiation stress values are 57.34 and 63.18% of that at 90°, respectively, and the peak strengths are 68.24 and 72.14% of that at 90°, which are only 19.79 and 26.65% higher than those of the fissured specimen of α = 0°. Based on the above analysis, there is a perforating azimuth dominance angle β ($30° \le \beta \le 45°$) in horizontal well fracturing. Selecting the dominant angle about perforation orientation, as shown in Figure 16, it is easier to form a large-scale complex crack network around the prefabricated fissure, break the effective reservoirs, and improve the discharge and production capacity. At the same time, it also provides a good solution to the superior arrangement of perforation orientation of horizontal well fracturing.

It is very important to clarify the initial structural characteristics, crack evolution law, and the mechanism of failure modes for reconstruction of the shale gas reservoir. In this paper, the mechanical properties and effects of the propagation process of the prefabricated (natural) fissure on shale specimens with horizontal bedding are studied experimentally, ignoring the influence of mechanical properties of bedding itself, lacking the research of crack evolution from the bedding angle, lacking the microscopic description of fracture surfaces, and lacking the verification and further study by using a numerical simulation. Therefore, how to better represent the instantaneous change of the shale matrix under load and simulate the failure process of the layered rock by using a discrete element method will be the focus of the next step of this study.

7. CONCLUSIONS

In this work, the mechanical properties, failure characteristics, and crack evolution of fissured shale were studied by a uniaxial compression test. The following conclusions can be drawn from the experiment:

(1) The pre-existing fissure will weaken the UCS of the specimens and peak strain. With the increase in α, the strength and peak strain increase but fall for α = 60° when the elastic modulus almost remains unchanged and the damage modulus slightly increases.

(2) For α = 0−90°, cracks initiated in the form of tensile cracks at the tip of the pre-existing fissure and the ultimate failure modes were mixed tensile-shear failure. With α increasing, the crack initiation angle and expansion angle first increase and then decrease.

(3) The pre-existing fissure makes the final cracks distributed around the tip of the pre-existing fissure, and the fissure in α = 30 and 45° plays an obvious role in forming a large-area crack network.

(4) The pre-existing fissure reduces the crack initiation stress that is positively correlated with α but decreases for α = 60°.

(5) The whole AE events are divided into four periods in which tensile cracks are dominant in the fissured specimens for α = 0−90°, but the proportion of shear cracks increases sharply after reaching the peak stress.

AUTHOR INFORMATION

Corresponding Author

Wei Liu − *State Key Laboratory of Coal Mine Disaster Dynamics and Control and School of Resources and Safety engineering, Chongqing University, Chongqing 400044, China;* orcid.org/0000-0003-0475-1023; Email: whrsmliuwei@126.com

Authors

Lin Li − *State Key Laboratory of Coal Mine Disaster Dynamics and Control and School of Resources and Safety engineering, Chongqing University, Chongqing 400044, China*

Yuehua Liu − *State Key Laboratory of Coal Mine Disaster Dynamics and Control and School of Resources and Safety engineering, Chongqing University, Chongqing 400044, China*

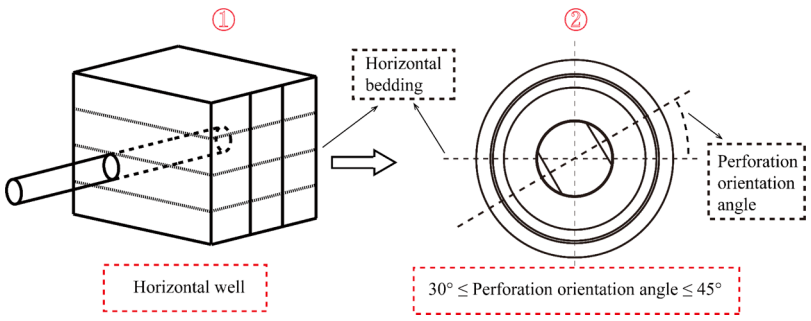

Figure 16. Selection of perforation orientation for horizontal well fracturing.

https://doi.org/10.1021/acsomega.1c03431
ACS Omega 2021, 6, 25461−25475

Xiong Zhang − *State Key Laboratory of Coal Mine Disaster Dynamics and Control and School of Resources and Safety engineering, Chongqing University, Chongqing 400044, China*

Jie Chen − *State Key Laboratory of Coal Mine Disaster Dynamics and Control and School of Resources and Safety engineering, Chongqing University, Chongqing 400044, China*

Deyi Jiang − *State Key Laboratory of Coal Mine Disaster Dynamics and Control and School of Resources and Safety engineering, Chongqing University, Chongqing 400044, China*

Jinyang Fan − *State Key Laboratory of Coal Mine Disaster Dynamics and Control and School of Resources and Safety engineering, Chongqing University, Chongqing 400044, China*

Complete contact information is available at: https://pubs.acs.org/10.1021/acsomega.1c03431

Notes

The authors declare no competing financial interest.

■ ACKNOWLEDGMENTS

The authors would gratefully like to acknowledge the financial support from the National Natural Science Foundation of China (nos. 52074046, 51904039, 51874273, 51774266, and 51834003), Chongqing Basic Research and Frontier Exploration Project (cstc2018jcyjAX0441), and Fundamental Research Funds for the Central Universities (nos. 2018CDQYZH0018 and Advances in Materials Science and Engineering 19cqu2018CDHB1B09), which are all greatly appreciated.

■ REFERENCES

(1) Cheng, Y.; Guo, Y.; Chen, G.; Yang, W.; Wang, F. On resource potential distribution and characteristics of shale gas in china. *J. Kunming Metall. Coll.* **2017**, *33*, 17−24.

(2) Men, X.; Han, Z.; Wang, L. History and current situation of shale gas exploration and development. *Xinjiang Pet. Geol.* **2018**, *39*, 372−376.

(3) Ling, K.; He, J.; Pei, P.; Ge, J.; Qin, W. A new correlation to evaluate the fracture permeability changes as reservoir is depleted. *J. Pet. Sci. Eng.* **2016**, *145*, 336−345.

(4) Ma, Y.; Zhong, N.; Yi, m.; Pan, Z. In Analysis of anisotropic permeability of Longmaxi shale and its influencing factors. In *The 10th National Petroleum Geology Experiment Technology Academic Exchange Conference*; Academic Press: Wuhan, 2016; pp. 1−2.

(5) Xin, Y.; Yao, J.; Li, L.; Gao, C.; Wen, Q. Optimization design of hydraulic fracturing process for shale gas horizontal wells. *Liaoning Chem. Ind.* **2017**, *46*, 284−287.

(6) Lei, M. *Study on the influence of perforation on the formation of fracture pattern around horizontal shale gas well*. Chengdu: Southwest Petroleum University, 2016.

(7) Liu, Q.; Wang, Q.; Guo, Q.; Li, H. Revelation of USshale gas exploration & development technology and management experience. *Mud Logging Eng.* **2012**, *23*, 33−36 40.

(8) Gong, T.; Xia, B.; Liu, L.; Peng, Z.; Gao, Y. Propagation of hydraulic fracture under the joint impact of bedding planes and natural fractures in shale reservoirs. *Energy Sci. Eng.* **2019**, *7*, 2690−2702.

(9) Jia, C.; Chen, Y.; Yang, C.; Xu, J.; Wang, L. Research on mechanical behaviors and failure modes of layer shale. *Rock Soil Mech.* **2013**, *34*, 57−61.

(10) Pan, L.; Cheng, L.; Zhang, S.; Guo, T.; Liu, K. Mechanism of fracture propagation via numerical stimulation of reservoir volume fracture in shale reservoirs. *Rock Soil Mech.* **2015**, *36*, 205−211.

(11) Lu, Y.; Zhou, J.; Li, H.; Chen, X.; Tang, J. Different Effect Mechanisms of Supercritical CO2 on the Shale Microscopic Structure. *ACS Omega* **2020**, *5*, 22568−22577.

(12) Lu, Y.; Chen, X.; Tang, J.; Li, H.; Zhou, L.; Han, S.; Ge, Z.; Xia, B.; Shen, H.; Zhang, J. Relationship between pore structure and mechanical properties of shale on supercritical carbon dioxide saturation. *Energy* **2019**, *172*, 270−285.

(13) Wang, Y.; Li, H.; Mitra, A.; Han, D.-H.; Long, T. Anisotropic strength and failure behaviors of transversely isotropic shales: An experimental investigation. *Interpret.* **2020**, *8*, SL59−SL70.

(14) Zuo, J.-P.; Li, Y.-L.; Liu, C.; Liu, H.-y.; Wang, J.; Li, H.-t.; Liu, L. Meso-fracture mechanism and its fracture toughness analysis of Longmaxi shale including different angles by means of M-SENB tests. *Eng. Fract. Mech.* **2019**, *215*, 178−192.

(15) Yin, H.; Zhou, J.; Xian, X.; Jiang, Y.; Lu, Z.; Tan, J.; Liu, G. Experimental study of the effects of sub- and super-critical CO 2 saturation on the mechanical characteristics of organic-rich shales. *Energy* **2017**, *132*, 84−95.

(16) Yang, Z. Y.; Chen, J. M.; Huang, T. H. Effect of joint sets on the strength and deformation of rock mass models. *Int. J. Rock Mech. Min. Sci.* **1998**, *35*, 75−84.

(17) Singh, M.; Rao, K. S.; Ramamurthy, T. Strength and deformational behaviour of a jointed rock mass. *Rock Mech.* **2002**, *35*, 45−64.

(18) Reik, G.; Zacas, M. Strength and deformation characteristics of jointed media in true triaxial compression. *Int. J. Rock Mech. Min. Sci. Geomech. Abstr.* **1978**, *15*, 295−303.

(19) Tian, W.; Liu, H. Insight into the Adsorption of Methane on Gas Shales and the Induced Shale Swelling. *ACS Omega* **2020**, *5*, 31508−31517.

(20) Sun, C. T.; Jin, Z. H., Griffith Theory of Fracture. In *Fracture Mechanics*; Academic Press: 2012; pp. 11−24, DOI: 10.1016/B978-0-12-385001-0.00002-X.

(21) Hoek, E.; Bieniawski, Z. T. Brittle fracture propagation in rock under compression. *Int. J. Fract. Mech.* **1965**, *1*, 276−155.

(22) Wei, M.-D.; Dai, F.; Falong, W.; Liu, Y.; Zhao, T. A novel chevron notched short rod bend method for measuring the mode I fracture toughness of rocks. *Eng. Fract. Mech.* **2018**, *190*, 1−15.

(23) Du, H.; Dai, F.; Xia, K.; Xu, N.; Xu, Y. Numerical investigation on the dynamic progressive fracture mechanism of cracked chevron notched semi-circular bend specimens in split Hopkinson pressure bar tests. *Eng. Fract. Mech.* **2017**, *184*, 202−217.

(24) Martin, C. D.; Chandler, N. A. The progressive fracture of Lac du Bonnet granite. *Int. J. Rock Mech. Min. Sci. Geomech. Abstr.* **1994**, *31*, 643−659.

(25) Xi, X.; Wu, X.; Guo, Q.; Cai, M. Experimental investigation and numerical simulation on the crack initiation and propagation of rock with pre-existing cracks. *IEEE Access* **2020**, *8*, 129636−129644.

(26) Li, Y.; Zhou, L.; Li, D.; Zhang, S.; Tian, F.; Xie, Z.; Liu, B. Shale Brittleness Index Based on the Energy Evolution Theory and Evaluation with Logging Data: A Case Study of the Guandong Block. *ACS Omega* **2020**, *5*, 13164−13175.

(27) Tang, H.-D.; Zhu, Z.-D.; Zhu, M.-L.; Lin, H.-X. Mechanical behavior of 3d crack growth in transparent rock-like material containing preexisting flaws under compression. *Adv. Mater. Sci. Eng.* **2015**, *2015*, 1−10.

(28) Yang, S.-Q.; Jing, H.-W. Strength failure and crack coalescence behavior of brittle sandstone samples containing a single fissure under uniaxial compression. *Int. J. Fract.* **2011**, *168*, 227−250.

(29) Yang, S.-Q.; Yang, Z.; Zhang, P.-C.; Tian, W.-L. Experiment and peridynamic simulation on cracking behavior of red sandstone containing a single non-straight fissure under uniaxial compression. *Theor. Appl. Fract. Mech.* **2020**, *108*, 102637.

(30) Liu, W.; Zhang, X.; Fan, J.; Zuo, J.; Zhang, Z.; Chen, J. Study on the mechanical properties of man-made salt rock samples with impurities. *J. Nat. Gas Sci. Eng.* **2020**, *84*, 103683.

(31) Li, X.; Peng, K.; Peng, J.; Hou, D. Effect of thermal damage on mechanical behavior of a fine-grained sandstone. *Arabian J. Geosci.* **2021**, *14*, 1212.
(32) Li, X.; Duan, Y.; Li, S.; Zhou, R. Study on the progressive failure characteristics of longmaxi shale under uniaxial compression conditions by x-ray micro-computed tomography. *Energies* **2017**, *10*, 1−13.
(33) Lajtai, E. Z. Shear strength of weakness planes in rock. *Int. J. Rock Mech. Min. Sci. Geomech. Abstr.* **1969**, *6*, 499−515.
(34) Arora, S.; Mishra, B. Investigation of the failure mode of shale rocks in biaxial and triaxial compression tests. *Int. J. Rock Mech. Min. Sci.* **2015**, *79*, 109−123.
(35) Liu, J.; Chen, Y.; Wan, W.; Wang, J.; Fan, X. The influence of bedding plane orientation on rock breakages in biaxial states. *Theor. Appl. Fract. Mech.* **2018**, *95*, 186−193.
(36) Wang, M.; Cao, P.; Wan, W.; Zhao, Y.-l.; Liu, J.; Liu, J.-s. Crack growth analysis for rock-like materials with ordered multiple pre-cracks under biaxial compression. *J. Cent. South Univ.* **2017**, *24*, 866−874.
(37) Liu, W.; Zhang, Z.; Fan, J.; Jiang, D.; Li, Z.; Chen, J. Research on gas leakage and collapse in the cavern roof of underground natural gas storage in thinly bedded salt rocks. *J. of Energy Storage* **2020**, *31*, 101669.
(38) Bobet, A.; Einstein, H. H. Fracture coalescence in rock-type materials under uniaxial and biaxial compression. *Int. J. Rock Mech. Min. Sci.* **1998**, *35*, 863−888.
(39) Bobet, A. The initiation of secondary cracks in compression. *Eng. Fract. Mech.* **2000**, *66*, 187−219.
(40) Wong, R. H. C.; Chau, K. T.; Tang, C. A.; Lin, P. Analysis of crack coalescence in rock-like materials containing three flaws—Part I: experimental approach. *Int. J. Rock Mech. Min. Sci.* **2001**, *38*, 909−924.
(41) Li, X.; Yang, S.; Wang, Y.; Nie, W.; Liu, Z. Macro-Micro Response Characteristics of Surrounding Rock and Overlying Strata towards the Transition from Open-Pit to Underground Mining. *Geofluids* **2021**, *2021*, 5582218.
(42) Zhang, Z.; Zhang, R.; Xie, H.; Liu, J.; Were, P. Differences in the acoustic emission characteristics of rock salt compared with granite and marble during the damage evolution process. *Environ. Earth Sci.* **2015**, *73*, 6987−6999.
(43) Zhu, Q.; Li, D.; Han, Z.; Li, X.; Zhou, Z. Mechanical properties and fracture evolution of sandstone specimens containing different inclusions under uniaxial compression. *Int. J. Rock Mech. Min. Sci.* **2019**, *115*, 33−47.
(44) Pan, J.; Wu, X.; Guo, Q.; Xi, X.; Cai, M. Uniaxial experimental study of the deformation behavior and energy evolution of conjugate jointed rock based on AE and DIC methods. *Adv. Civ. Eng.* **2020**, *2020*, 1−16.
(45) Jiang, D.; Xie, K.; Chen, J.; Zhang, S.; Tiedeu, W. N.; Xiao, Y.; Jiang, X. Experimental Analysis of Sandstone Under Uniaxial Cyclic Loading Through Acoustic Emission Statistics. *Pure Appl. Geophys.* **2019**, *176*, 265−277.
(46) Ganne, P.; Vervoort, A.; Wevers, M. Quantification of pre-peak brittle damage: Correlation between acoustic emission and observed micro-fracturing. *Int. J. Rock Mech. Min. Sci.* **2007**, *44*, 720−729.
(47) Huang, Y.-H.; Yang, S.-Q.; Tian, W.-L.; Zeng, W.; Yu, L.-Y. An experimental study on fracture mechanical behavior of rock-like materials containing two unparallel fissures under uniaxial compression. *Acta Mech. Sin.* **2016**, *32*, 442−455.
(48) Zhang, X.; Liu, W.; Jiang, D.; Qiao, W.; Liu, E.; Zhang, N.; Fan, J. Investigation on the influences of interlayer contents on stability and usability of energy storage caverns in bedded rock salt. *Energy* **2021**, *231*, 120968.
(49) Mousavi Nezhad, M.; Fisher, Q. J.; Gironacci, E.; Rezania, M. Experimental Study and Numerical Modeling of Fracture Propagation in Shale Rocks During Brazilian Disk Test. *Rock Mech.* **2018**, *51*, 1755−1775.
(50) Lu, Y.; Xu, Z.; Li, H.; Tang, J.; Chen, X. The influences of super-critical CO2 saturation on tensile characteristics and failure modes of shales. *Energy* **2021**, *221*, 119824.
(51) Morris, K.; Rosenkranz, A.; Seibert, H.; Ringel, L.; Diebels, S.; Talke, F. E. Uniaxial and biaxial testing of 3D printed hyperelastic photopolymers. *J. Appl. Polym. Sci.* **2020**, *137*, 48400.
(52) Duan, Y. T.; Li, X.; Ranjith, P. G.; Wu, Y. F. An investigation of the evolution of the internal structures and failure modes of Longmaxi shale using novel X-ray microscopy. *J. Pet. Sci. Eng.* **2020**, *184*, 106479.
(53) Duan, Y.; Li, X.; Zheng, B.; He, J.; Hao, J. Cracking Evolution and Failure Characteristics of Longmaxi Shale Under Uniaxial Compression Using Real-Time Computed Tomography Scanning. *Rock Mech.* **2019**, *52*, 3003−3015.
(54) Kawakata, H.; Cho, A.; Yanagidani, T.; Shimada, M. The observations of faulting in westerly granite under triaxial compression by X-ray CT scan. *Int. J. Rock Mech. Min. Sci.* **1997**, *34*, 151.e1−151.e12.
(55) Asadizadeh, M.; Tavakoli, H.; Rahmannejad, R.; Mehinrad, A. Effect Of Anisotropy And Confining Pressure Ratio On Rock Mass Deformation Modulus At Bakhtiary Dam Site (Iran). *ISRM International Symposium - 6th Asian Rock Mechanics Symposium*, 2010.
(56) Okano, S.; Matsuo, K.; Nomura, M.; Obara, K.; Yamachi, H. Considerartion of the relative behavior between cable bolts and rock masses installed into the tunnel face. *Proc. Eng., Jsce* **1996**, *6*, 157−162.
(57) CE, F.; JA, H. Draft proposed isrm method for determination of complete rock stress-strain curves by uniaxial compression tests. *Chin. J. Rock Mech. Eng.* **2000**, *6*, 802−808.
(58) Li, Z.; Jia, C.; Yang, C.; Zeng, Y.; Guo, Y.; Heng, S.; Wang, L.; Hou, Z. Propagation of hydraulic fissures and bedding planes in hydraulic fracturing of shale. *Chin. J. Rock Mech. Eng.* **2015**, *34*, 13−20.
(59) Xin, C.; Xi, P.; Dongwei, L.; Wentao, L. Analysis on cracking mechanism of fractured rock masses under uniaxial compression based on the two cracking criteria. *Eng. Mech.* **2013**, *30*, 227−235.
(60) Image-J software v1.8.0. document. *https://imagej.net/docs/guide/*.
(61) Wang, H.; Li, Y.; Cao, S.; Pan, R.; Yang, H.; Zhang, K.; Liu, Y. Brazilian splitting test study on crack propagation process and macroscopic failure mode of pre-cracked black shale. *Chin. J. Rock Mech. Eng.* **2020**, *39*, 912−926.
(62) Matlab R2018b document. *https://www.mathworks.com/help/matlab/index.html*.
(63) Meng, Q.; Zhang, M.; Han, L.; Pu, H.; Chen, Y. Acoustic Emission Characteristics of Red Sandstone Specimens Under Uniaxial Cyclic Loading and Unloading Compression. *Rock Mech.* **2018**, *51*, 969−988.
(64) Eberhardt, E.; Stead, D.; Stimpson, B. Quantifying progressive pre-peak brittle fracture damage in rock during uniaxial compression. *Int. J. Rock Mech. Min. Sci.* **1999**, *36*, 361−380.
(65) Guo, C.; Qin, L.; Li, D.; Zhou, D. Effect of Ground Stress and Initial Fissure on Crack Initiation Direction and Pressure by Hydraulic Fracturing. *Saf. Coal Mines* **2015**, *46*, 161−165.
(66) Yin, P.; Yang, S.; Zeng, W. A simulation study on strength and crack propagation characteristics of composite rock strata with single fracture. *J. Basic Sci. Eng.* **2015**, *23*, 608−621.
(67) Feng, H.; Jia, Y.; Xu, Z.; Cao, J.; Wu, G. Optimization of multi-stage and multi-cluster fracturing technology for horizontal wells in jilantai buried hill. *IOP Conf. Ser.: Earth Environ. Sci.* **2021**, *634*, 012142.

https://doi.org/10.1021/acsomega.1c03431
ACS Omega 2021, 6, 25461−25475